MICRO-SCALE ANALYSIS OF ROUGH SURFACES USING NON-CONFORMING MESHES

MARTA C. OLIVEIRA[*], DIOGO M. NETO[*], PEDRO J. COSTA[*] AND LUÍS F. MENEZES[*]

[*] Centre for Mechanical Engineering, Materials and Processes (CEMMPRE)
ARISE, Department of Mechanical Engineering, University of Coimbra
Pinhal de Marrocos, 3030-788 Coimbra, Portugal
email: {marta.oliveira; diogo.neto; pedro.costa; luis.menezes}@dem.uc.pt, https://www.uc.pt/

Key words: Finite element method, Surface topography, Surface roughness, Normal contact, Elasto-plasticity.

Summary. This work presents a finite element model of the contact between a flat rigid surface and a rough deformable elastoplastic body, enabling the micro-scale analysis of the contact conditions. To assure the computational efficiency a non-conforming mesh is adopted to describe the deformable body. The results show that the model can capture the main effects of the bulk material constitutive behaviour, which is known to have a significant impact on the problem, as well on local changes on the friction conditions.

1 INTRODUCTION

Contact problems are known for their high level of complexity, even when avoiding lubricated conditions. The behaviour of the contacting surfaces is dictated by parameters such as the elastoplastic properties of both solid surfaces and their surface characteristics, such as roughness or chemical bonding. Solid lubricants, which are materials that, despite being in the solid phase, can reduce friction between two surfaces sliding against each other, without the need for a liquid lubricant. In that case, during sliding contact, structural transformations and/or chemical reactions occurs, which generate locally a tribolayer (tribological layer) with low friction properties [1]. They are known as self-adaptive low friction coatings. Unfortunately, tribological tests indicate that the formation of the tribolayer is very sensitive to the sliding contact conditions, contributing to inconsistent results in industrial applications. Numerical models at the micro-scale can be used to try to improve the understanding about the conditions for the formation of the tribolayer, combined with an experimental approach.

In this context, this work presents a preliminary work that focuses on evaluating the potential of using non-conforming meshes for the analysis of contact problems for rough surfaces, to reduce the computational time. The finite element model was built in DD3IMP finite element code [2]. The following section describes the main features of the model, which considers the contact between a flat rigid surface and a deformable body with a rough surface.

2 FINITE ELEMENT MODEL

The selected Representative Contact Element (RCE) presents a rough surface, which is assumed to be in contact with a rigid flat surface, controlled with a prescribed displacement. The RCE opposite surface to the contact one has fixed displacements, while symmetry boundary conditions are assumed for the other surfaces, as schematically shown in Figure 1 (a). These boundary conditions are imposed as shown in Figure 1 (b), based on the principle of master and slave edges and nodes as suggested in [3].
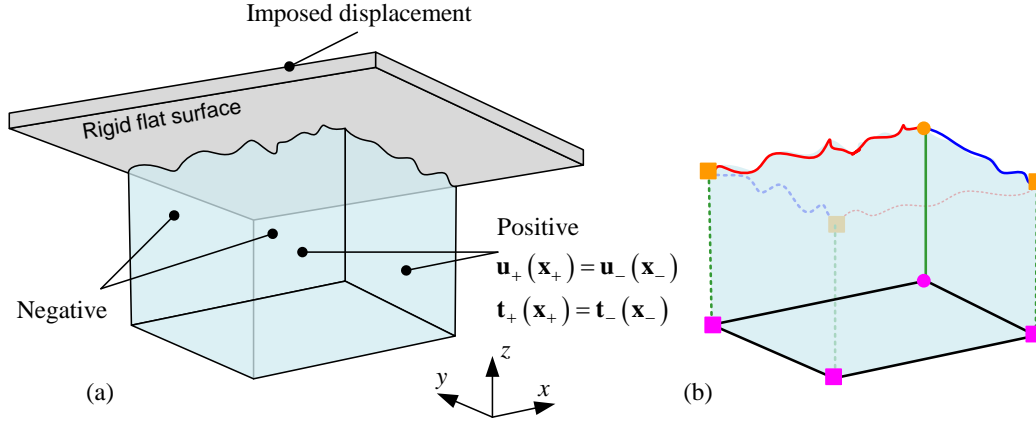

Figure 1: (a) Numerical setup for the RCE and (b) Master-slave conditions of the RCE - master (continuous lines and circles); slaves (dashed lines and squares) (adapted from [3])

2.1 Constitutive model

The RCE is considered homogeneous body with elasto-plastic behaviour. The elastic regime is assumed isotropic, described by the Hooke's law, considering the Young modulus, $E = 100$ GPa, and the Poisson ratio, $\nu = 0.3$. The plastic behaviour is assumed also has isotropic, described by the von Mises yield criterion:

$$(\sigma_{yy} - \sigma_{zz})^2 + (\sigma_{zz} - \sigma_{xx})^2 + (\sigma_{xx} - \sigma_{yy})^2 + 6\tau_{yz}^2 + 6\tau_{xz}^2 + 6\tau_{xy}^2 = 2Y^2 , \qquad (1)$$

written in function of the components of the Cauchy stress tensor, $\boldsymbol{\sigma}$, in the coordinate system, $Oxyz$, and of the flow stress, Y. Moreover, for one example, the plastic behaviour is assumed to be transversely isotropic, described with the aid of the Hill'48 yield criterion [4]:

$$F(\sigma_{yy} - \sigma_{zz})^2 + G(\sigma_{zz} - \sigma_{xx})^2 + H(\sigma_{xx} - \sigma_{yy})^2 + 2L\tau_{yz}^2 + 2M\tau_{xz}^2 + 2N\tau_{xy}^2 = Y^2 , \qquad (2)$$

where F, G, H, L, M and N are material parameters. To consider the transversely isotropic behaviour $F = G$, $G + H = 1$ and the parameters $L = M = N$ assume the isotropic value of 1.5 (see Eq. (1)). For decreasing values of $F = G$ the ratio between the flow stress along the $Ox = Oy$ orientation and the through-thickness one, Oz, increases. In the example considered $F = G = 0.32$, which leads to an initial yield stress along the through-thickness direction 1.25 times greater than the one along $Ox = Oy$ orientation. The material is assumed to be perfectly plastic, with a yield stress Y_0 of 1 GPa, as shown in Figure 2 (a). Figure 2 (b) presents the yield surfaces for biaxial stress conditions in the Oxy plane, highlighting that for the transversely

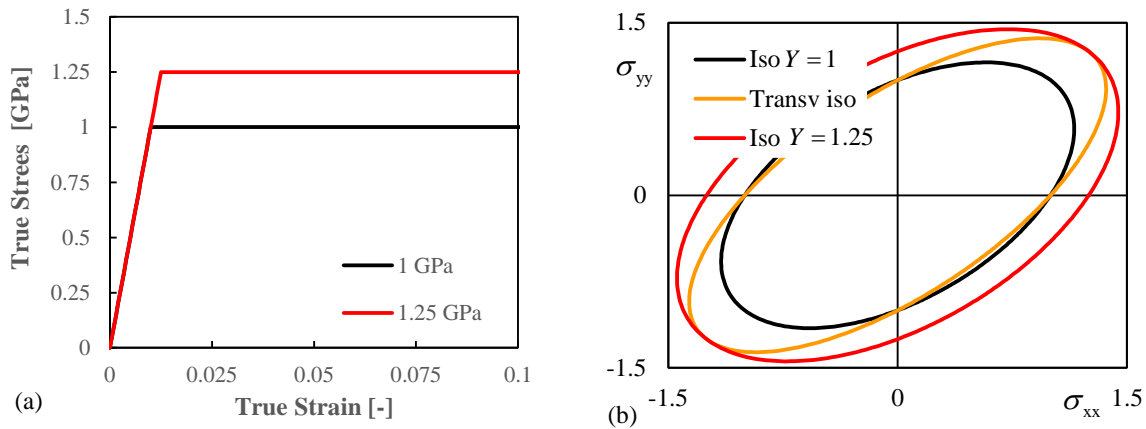isotropic material the equibiaxial yield stress is equal to the through-thickness one, i.e., 1.25 GPa.

Figure 2: Plastic behaviour: (a) True stress versus strain evolution and (b) Yield surface: isotropic (von Mises), yield stress of 1.0 and 1.25 GPa, and transversely isotropic (Hill'48)

2.2 Spatial discretization

The flat surface is assumed rigid, and it is described as a single Nagata patch [5]. The RCE is discretized with solid elements, i.e. 8 node linear hexahedron finite elements, combined with a selective reduced integration technique. The RCE considered in this work is a cube with 4 μm × 4 μm, based on the reference results that consider that dimensions should be a function of the topography roughness [3]. The cube is initially discretized with a uniform mesh and then the top layer finite element density is increased, using a non-conforming mesh as transition scheme, as shown in Figure 3 (a). This approach assures an accurate description of the roughness characteristics while maintaining admissible computation times. The use of a non-conforming mesh leads to the presence of hanging nodes, whose degrees-of-freedom are defined as linear combinations of degrees-of-freedom of neighbouring regular nodes. The treatment of these hanging nodes is performed considering the Lagrange Multiplier method. For the example adopted in this study, the cube has a total of 152,916 elements (220,506 nodes), corresponding to a total of 66,049 nodes (257 x 257) in the contact surface, i.e., ~30% of the total. The contact with the rigid flat surface is assumed to be frictionless or described by the Coulomb friction model, which is solved using the Augmented Lagragian Method.

The quantitative characterization of the surface topography was performed using Power Spectral Decomposition (PSD), with the surface generator code proposed in [6], for artificial randomly rough Gaussian surfaces [7]. The input parameters considered were: (1) the root-mean-square roughness (R_q), i.e. standard deviation of surface heights (σ); (2) the Hurst exponent (H), which is related to the fractal dimension of a surface topography $D = 3 - H$; (3) the length of final topography/image, L_x in the Ox direction; (4) m and n, which are the number of pixels in the Ox/Oy direction of final topography/image, respectively, and (5) the roll-off wavevector, q_r. The values selected for the examples discussed in the following section are summarized in Table 1 and correspond to typical values found in literature. Since the surface under study has isotropic roughness characteristics, the derived radial average on the calculated

discrete Fourier transform of the surface topography was used to obtain its 2D power spectrum, as shown in Figure 3 (c).
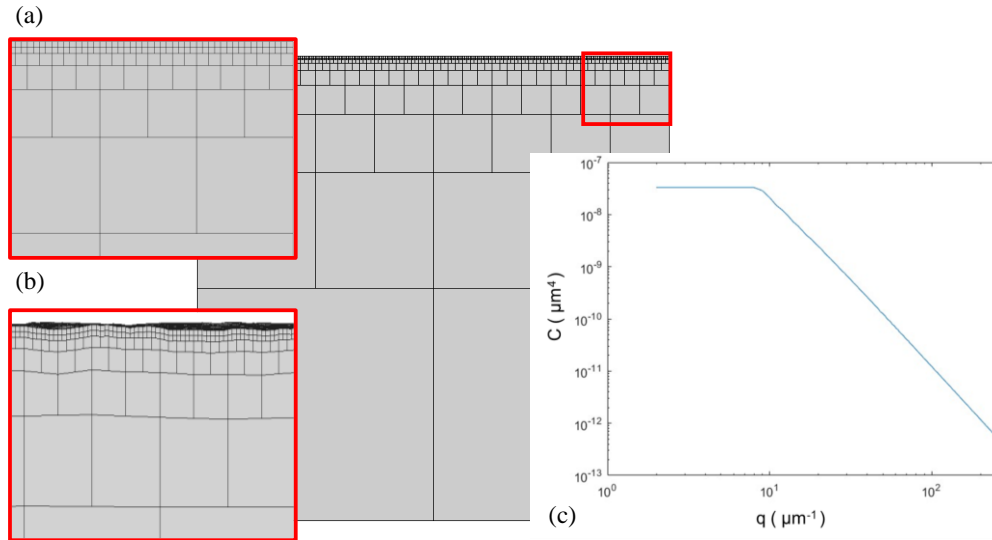

Figure 3: Mesh adopted for the representative contact element including detail of the surface: (a) before and (b) after including the roughness description. (c) Radially averaged 2D PSD of the surface presented in (b) [6]

Table 1: Parameters adopted in the surface generator code proposed in [6, 7]

Root-mean-square roughness (R_q)	5×10^{-3} [µm]
Hurst exponent (H)	0.7
Length of final topography (L_x)	4 [µm]
Number of pixels in the Ox/Oy directions ($m=n$)	257
Cut-off wavevector (q_r)	10 [1/ µm]

2.3 Contact area and pressure evaluation

The Augmented Lagrangian method adopted to solve the contact problem calculates the contact force for each node. This variable is evaluated in a local frame associated with the contact node, based in the normal direction to the contact surface. Thus, the node normal contact force defined in the local frame, λ^n, is known for each increment. To estimate the contact pressure, it is necessary to evaluate the area of influence of the node, $A_{final}^{[node]}$.

In this work, the real contact area is evaluated based on geometrical considerations, considering the contact status of neighbouring nodes, as suggested by [8], but also considering the normal distance of the node to the contact surface. The first step is to identify all the finite elements sharing the node in contact, as well as all potential contact nodes of those finite elements. Figure 4 (a) presents, in a two-dimensional scheme, all potential contact nodes associated with four finite elements, which share node 4. These are the nodes necessary to evaluate the contact area associated with node 4 in the same figure. The facet area of each element, $A^{(e)}$, can be evaluated from the nodal coordinates of the four vertex nodes. A value

4

corresponding to a quarter of this facet area is assigned to each node of the element, $A^{[node]} = 0.25A^{(e)}$. For instance, considering that the facet area of element 1 is $A^{(1)}$, then $0.25A^{(1)}$ corresponds to the apparent contact area of node 4, if all nodes of element 1 are in contact with the surface (grey area in Figure 4 (b)). However, if every node of element 1 are not in contact it is necessary to introduce a correction factor to this area, as presented by the dark area in Figure 4 (b). This correction function should consider the distance of neighbouring nodes (gap status) to the surface. Figure 4 (c) and (d) exemplifies two situations for which nodes 3 and 6 present gap contact status. However, in the case of Figure 4 (c) although the nodes have no contact force, since the normal contact distance is null, no correction should be performed to the contact area. On the other hand, the contact area must diminish for increasing values of the normal distance value of the adjacent nodes (Figure 4 (d)). The correction function used was proposed in [9] and is given by:

$$A_{corr}^{[node]} = \frac{1}{2}\left(1 + \frac{\sum_{k=1}^{nct} c_t}{nct}\right) A^{[node]}$$

$$\text{with } c_t = \begin{cases} 1, & \text{if node } k \text{ in contact or } d^n = 0 \\ \dfrac{1}{d^n + 1}, & \text{if node } k \text{ gap} \end{cases}$$ (3)

where nct corresponds to the total number of potential contact nodes of the finite element, containing the node for which the correction function is being calculated. For hexahedral finite elements nct is equal to 3. This procedure is repeated for each finite element to which the node belongs. At the end the contact area of the node is calculated as:

$$A_{final}^{[node]} = \sum_{i=1}^{el} A_{corr}^{[node]},$$ (4)

where el is the total number of finite elements to which the node belongs. The contact pressure is calculated as the ratio between the normal contact force and the estimated contact area:

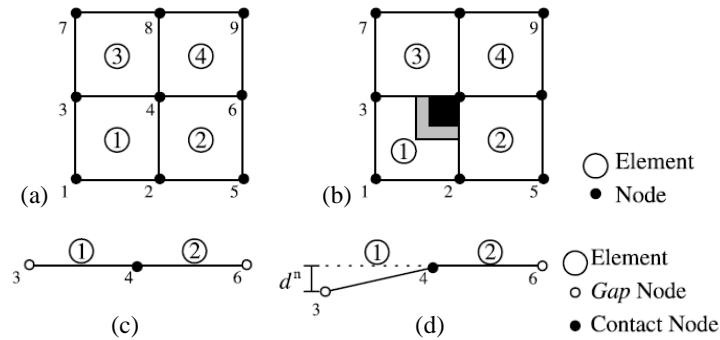$$p^{[node]} = \lambda^n / A_{final}^{[node]}.$$ (5)

Figure 4: Schematic representation of the geometrical evaluation of contact area for node 4: (a) neighbouring elements, (b) contact area for element 1, (c) neighbouring nodes with gap status but null normal distance and (d) neighbouring nodes with gap status and non-null normal distance [9]

5

3 RESULTS ANALYSIS AND DISCUSSION

Numerical simulations were conducted with the RCE submitted to compression by the flat surface, until attaining a displacement of 0.1 μm. Table 2 presents the summary of the test conditions considered, which will be analysed in this section.

Table 2: Resume of the test conditions and labels

Label	Yield stress [GPa]	Friction coefficient [-]	Yield criterion
Y1	1.0	0.0	von Mises
Y1_0.1	1.0	0.1	von Mises
Y1.25	1.25	0.0	von Mises
Y1_1.25	1.0	0.0	Hill'48

3.1 Contact area and average pressure

Figure 5 (a) presents the evolution of the normalized contact area, i.e., the ratio between the effective contact area, A, evaluated using Eq. (4), and the apparent contact area, A_0. The evolution is presented in function of the average pressure, $\bar{p}$, which corresponds to the total force applied by the flat surface divided by A_0. This evolution is almost linear, until a normalized contact area of ~0.3, followed by a non-linear behaviour, as reported in previous works [10]. Both the regimes are affected by the plastic behaviour of the material, mainly the yield stress.
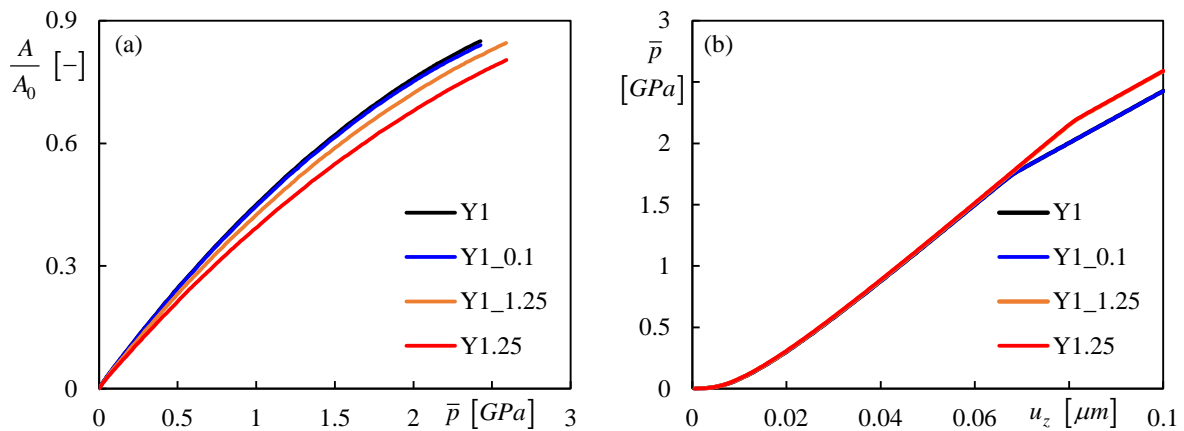

Figure 5: (a) Evolution of the normalized contact area in function of the average pressure and (b) Evolution of the average pressure in function of the imposed displacement.

The isotropic material with a higher yield stress leads to a smaller normalized contact area when submitted to the same average pressure. This is related with the fact that the asperities will enter the plastic regime for higher values of average pressure, which also explains the fact that a higher average pressure is attained at the end. Interestingly, the average contact pressure as a similar evolution with the displacement of the flat surface for the isotropic material with the higher yield stress and the transversely isotropic material (see Figure 5 (b)), confirming the influence of the yield stress for the normal (compression) direction. The same occurs for the

6

tests performed with the same material properties, with or without friction. Nevertheless, the normalized contact area evolves differently for the transversely isotropic material, highlighting also the impact of the yield stress for the biaxial (compression) direction, while the presence of friction has a negligeable effect. Figure 5 (a) confirms that, at the end of the test, the transversely isotropic material (Y1_1.25) presents a normalize contact area more like the one observed for the isotropic material with a smaller yield stress (Y1), related with the higher average pressure (see Figure 5 (b)).

3.2 Pressure distribution

Figure 6 presents the pressure distribution on the RCE surface for the total displacement of the flat surface of 0.1 μm, for the four test conditions under analysis. The figure highlights the similarities for the tests performed considering only different values of the friction coefficient. Nevertheless, it is possible to confirm the influence of the contact with friction in the slightly smaller values of equivalent plastic strain attained when considering the friction coefficient value of 0.1, when compared with the frictionless condition (see Figure 7, Y1 maximum value of 0.31 and Y1_0.1, 0.25). On the other hand, higher local contact pressures are attained for the isotropic material with the higher yield stress, which correspond to smaller values of equivalent plastic strain (maximum value of 0.27) when compared with Y1, as shown in Figure 7. This is a consequence of assuming the same elastic behaviour, as shown in Figure 2. Figure 6 also shows that the material with transversely isotropic behaviour presents local contact pressure values higher than the isotropic with a yield stress of 1 GPa and lower than the one with 1.25 GPa. This is associated with slightly higher values of equivalent plastic deformation for the transversely isotropic material (maximum value of 0.32) than the isotropic ones (see Figure 7).
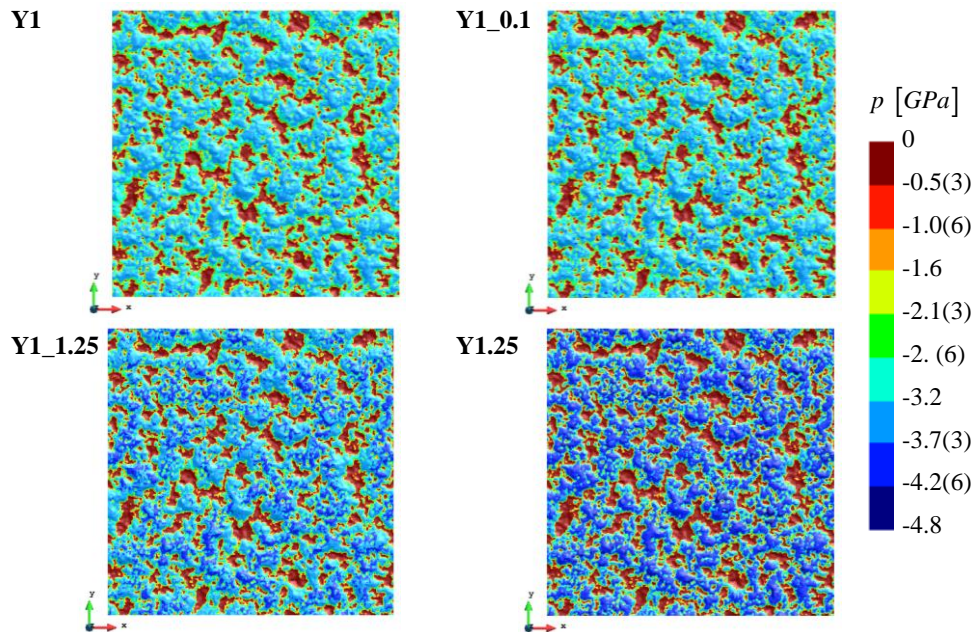

Figure 6: Distribution of the local contact pressure for a displacement of the flat surface of 0.1 μm

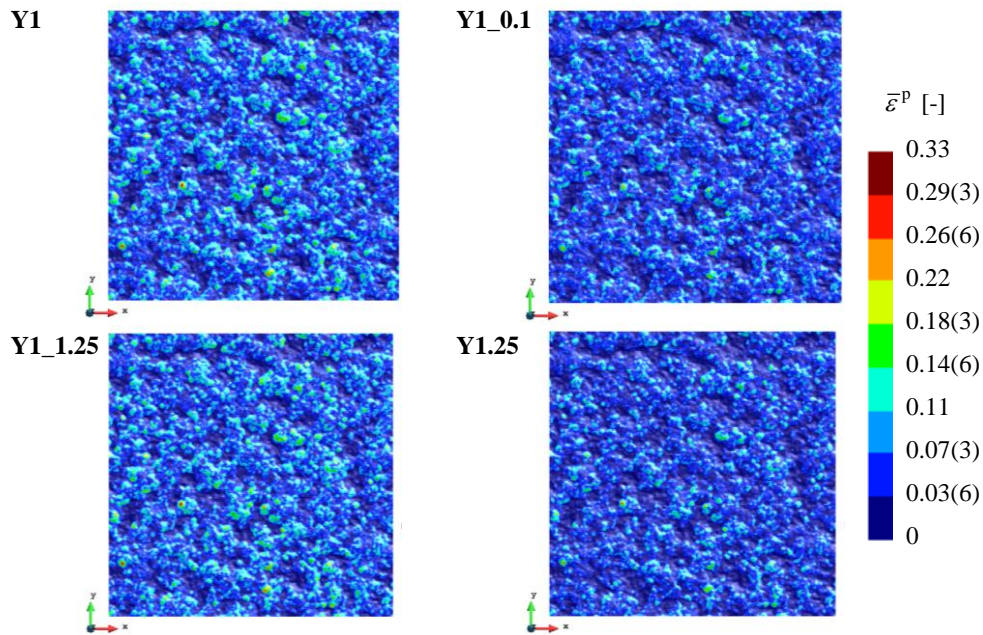**Figure 7**: Distribution of the equivalent plastic strain for a displacement of the flat surface of 0.1 μm

Figure 8 presents the evolution of the distribution of the local pressure values with the displacement of the flat surface. To facilitate the analysis, the total number of nodes of the surface with a certain value of local contact pressure was normalized by the total number of nodes of the surface (66,049), to present the frequency percentage. Moreover, the nodes with no contact pressure are also separated. The analysis of this figure highlights that, even for a small displacement of the flat surface of 0.2 μm, there are already some nodes submitted to pressure values higher than the yield stress, even though approximately 85% of the contact surface nodes are not in contact. With the increase of the displacement of the flat surface, the number of nodes not in contact reduces, until attaining approximately 15%, except for the isotropic material, which present approximately 20%. In fact, when analysing the distribution for the isotropic material Y1, for a displacement of 1 μm, approximately 35% of the nodes present a local pressure value between 3.0 and 3.5 GPa. The trend is quite similar for the test conditions considering a friction coefficient of 0.1 and the frictionless case. Nevertheless, it is possible to confirm that by restraining the material movement, a higher number of nodes tends to present higher values of local contact pressure. The influence of the yield stress is clearly visible not only in the contact pressure range (see Figure 6), but also on its distribution. Note that for Y1.25 there is a more even distribution of the number of contact nodes with a certain value of contact pressure, when compared with the Y1 case. This also correlates with the lower values of maximum equivalent plastic strain, reported for Y1.25, when compared with Y1. On the other hand, the transversely isotropic material, is the one presenting a more uneven distribution of the number of nodes submitted to a certain local contact pressure value, which can help to explain the highest values of maximum equivalent plastic strain.
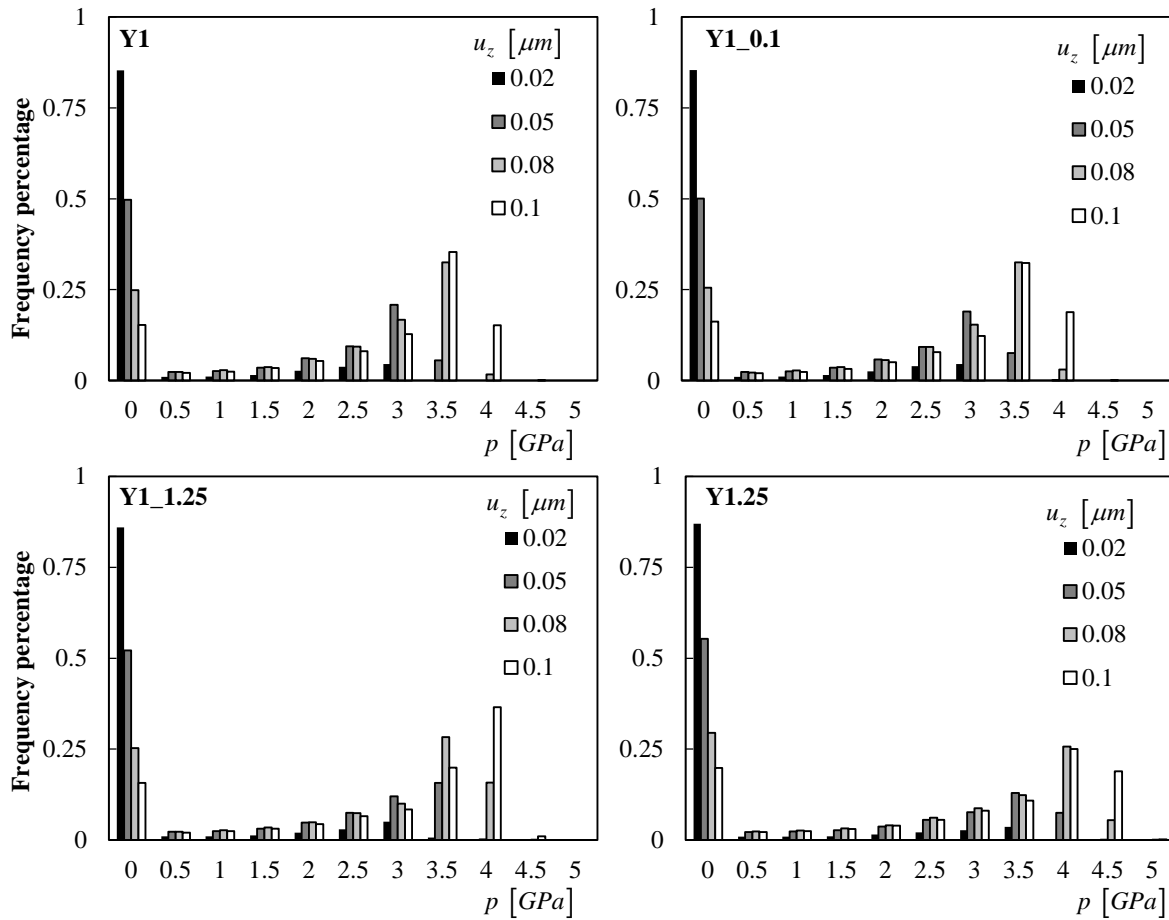
Figure 8: Frequency percentage of pressure values in function of the displacement of the flat surface

3.2 Roughness evaluation

In this section, the evolution of the contact surface roughness is discussed only for the isotropic materials with a yield stress of 1 GPa. Figure 9 presents the height distribution for the original surface, highlighting the maximum value for the peaks and the valleys of 0.02 μm. This correlates well with the fact that for a displacement of 0.02 μm of the flat surface there is already plastic deformation of the asperities, leading to contact pressure values higher than the yield stress (see Figure 8). As shown in Figure 9, for a displacement of 0.05 μm of the flat surface the peaks become negligible, and the surface becomes even more uniform with the increase of the displacement. In fact, the tensile stress in the through-thickness direction, induced on the valleys by the plastic deformation of the asperities, also contribute to the reduction of their height.
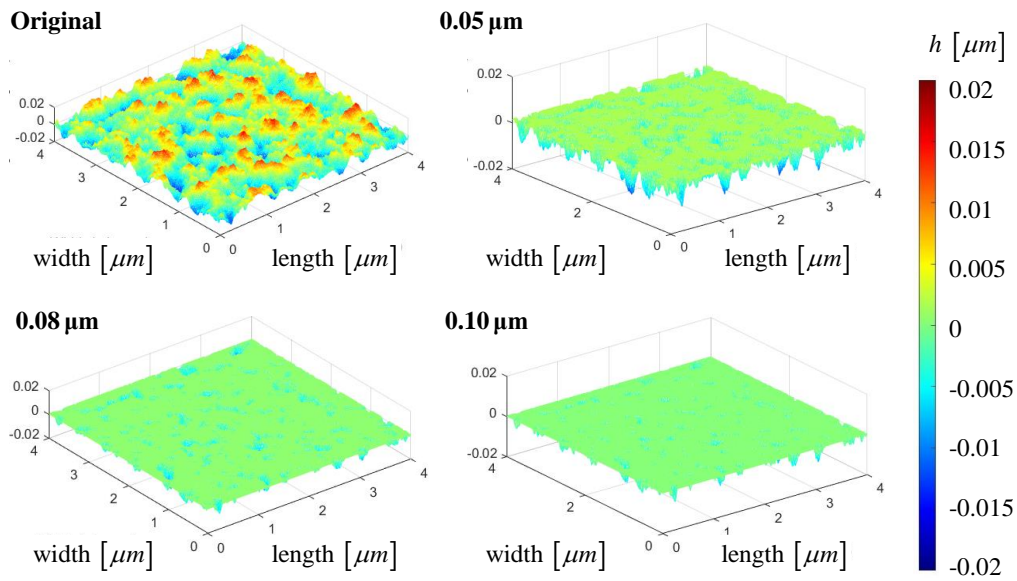
9

Figure 9: Evolution of the surface height in function of the flat surface displacement, for the isotropic material with a yield stress of 1 GPa
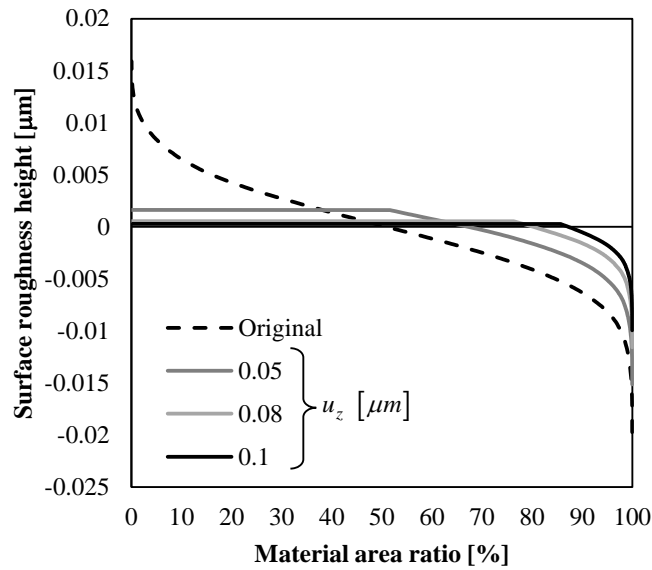

Figure 10: Abbott-Firestone curve evaluated for the original surface and for the ones obtained after a fixed displacement of the flat surface, for the isotropic material with a yield stress of 1 GPa

   To quantify this effect, the Abbott-Firestone curve of each of the surface roughness presented in Figure 9 was evaluated and are compared in Figure 10. The void volume in the valleys zone of the original surface corresponds to 11% for a normalized contact area of 84%, according to the procedure defined in [11]. For a displacement of 0.05 μm, it decreases to 10% for a normalized contact area of 52%. This value reduces to 4%, corresponding to a normalized contact area of 76%, for the displacement of 0.08 μm and to 2%, for a normalized contact area

of 85%, for the final displacement of 0.1 μm. It should be mentioned that the surfaces were extracted for the loaded RCE. Nevertheless, for the final displacement of 0.1 μm, the surface was also unloaded. Figure 11 (a) presents the distribution of the Cauchy stress components σ_{zz} before the unloading, highlighting the uniform value of -2.42 GPa away from the top surface, which correlates with the results shown in Figure 5. After unloading, the RCE presents a null σ_{zz} component, except on the top surface were the former peaks still present compressive residual stresses and the valleys tensile ones, as shown in Figure 11 (b). The plastic deformation induced on the surface leads to a negligible effect of the unloading on the predicted contact surface topography.
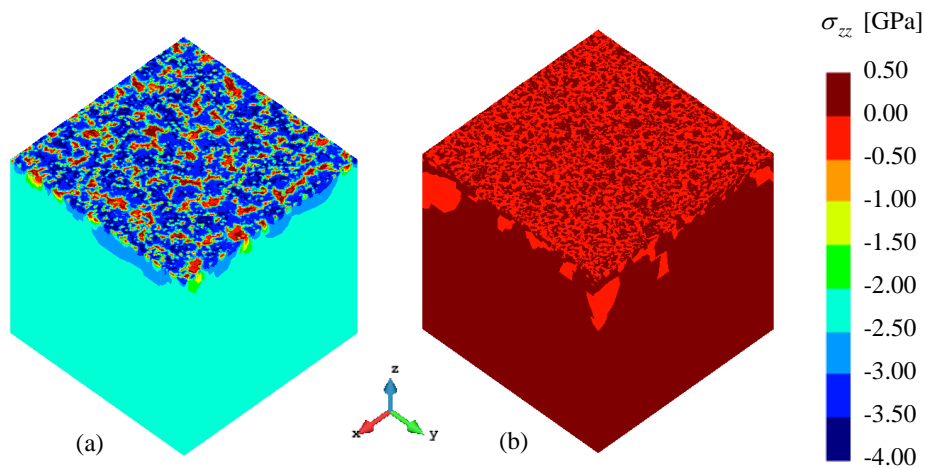

Figure 11: Distribution of the σ_{zz} stress component on the RCE: (a) for a flat surface displacement of 0.1 mm and (b) unloaded, for the isotropic material with a yield stress of 1 GPa

4 CONCLUSIONS

The finite element model resorting to a non-conforming mesh enables capturing the main effects of the bulk material constitutive behaviour, with the saturation character on the material stress response being reflected on the contact pressure, changing the contact pressure distribution, and the rate of change of the contact area fraction. The changes on the friction coefficient have a slight impact on the local contact pressure but a more relevant one on the level of equivalent plastic strain. The fact that the material is restrained from deforming due to the "stick" contact status leads to smaller values of the maximum equivalent plastic strain.

The relationship between the applied pressure (average) and the effective contact area is not linear, as reported in previous works. The effective contact area is evaluated based on a strategy that considers the nodes contact status and their distance to the flat rigid surface. The results shown that the effective contact area attains values close to about 50% of the apparent contact area when the applied pressure (average) is approximately the yield stress, Finally, the analysis of the deformed rough surface shows that the contact with the rigid surface eliminates the peaks while reducing the void volume in the valleys zone.

ACKNOWLEDGEMENTS

REFERENCES

[1] Yaqub, T. Bin, Bruyere, S., Pierson, J. F., Vuchkov, T., and Cavaleiro, A. 2020, "Insights into the Wear Track Evolution with Sliding Cycles of Carbon-Alloyed Transition Metal Dichalcogenide Coatings," Surf Coat Technol, 403, p. 126360. https://doi.org/10.1016/J.SURFCOAT.2020.126360

[2] Menezes, L.F., Teodosiu, C. 2000, "Three-dimensional numerical simulation of the deep-drawing process using solid finite elements", J Mater Process Technology, 97(1-3), p. 100–106. https://doi.org/10.1016/S0924-0136(99)00345-3

[3] Pinto Carvalho, R., Couto Carneiro, A. M., Andrade Pires, F. M., and Doca, T. 2022, "An Efficient Multiscale Strategy to Predict the Evolution of the Real Contact Area between Rough Surfaces," Tribol Int, 165. https://doi.org/10.1016/j.triboint.2021.107255

[4] Hill, R. 1948, "A Theory of the Yielding and Plastic Flow of Anisotropic Metals," Proceedings of the Royal Society of London A: Mathematical, Physical and Engineering Sciences, 193(1033). https://doi.org/10.1098/rspa.1948.0045

[5] Neto, D. M., Oliveira, M. C., Menezes, L. F., and Alves, J. L. 2014, "Applying Nagata Patches to Smooth Discretized Surfaces Used in 3D Frictional Contact Problems," Comput Methods Appl Mech Eng, 271. https://doi.org/10.1016/j.cma.2013.12.008

[6] Mahboob Kanafi, M. 2024. "Surface generator: artificial randomly rough surfaces" https://www.mathworks.com/matlabcentral/fileexchange/60817-surface-generator-artificial-randomly-rough-surfaces, MATLAB Central File Exchange.

[7] Mahboob Kanafi, M., and Tuononen, A. J. 2017, "Top Topography Surface Roughness Power Spectrum for Pavement Friction Evaluation," Tribol Int, 107, pp. 240–249. https://doi.org/10.1016/j.triboint.2016.11.038

[8] Tanner, J. A. 1996, "Computational Methods for Frictional Contact With Applications to the Space Shuttle Orbiter Nose-Gear Tire Development of Frictional Contact Algorithm". https://ntrs.nasa.gov/api/citations/19960017561/downloads/19960017561.pdf

[9] Oliveira, M. C., Alves, J. L., and Menezes, L. F. 2008, "Algorithms and Strategies for Treatment of Large Deformation Frictional Contact in the Numerical Simulation of Deep Drawing Process," Archives of Computational Methods in Engineering, 15(2), pp. 113–162. https://doi.org/10.1007/s11831-008-9018-x

[10] Persson, B. N. J. 2022, "Functional Properties of Rough Surfaces from an Analytical Theory of Mechanical Contact," MRS Bull, 47(12), pp. 1211–1219. https://doi.org/10.1557/s43577-022-00472-6

[11] ISO 25178-2 (GPS) — Surface Texture: Areal — Part 2: Terms, Definitions and Surface Texture Parameters.